Sampling Time Modulation of a Photovoltaic Power Tracking Controller Based Upon Real-Time Monitoring of Converter Dynamics

Vinay Kumar Kolakaluri, Mohammad Nair Aalam, and Vaskar Sarkar, *Member, IEEE*

***Abstract*—The maximum power point tracking (MPPT) or flexible power point tracking (FPPT) of a photovoltaic (PV) array is typically performed by using a discrete-time control system. The sampling time of an MPPT/FPPT controller plays a crucial role in determining its transient performance. Performing the MPPT or FPPT control at a fixed sampling rate makes it necessary to set the respective sampling time to a large value so as to effectively deal with the worst case of converter transient. This, in turn, makes the power tracking continue for an unnecessarily longer time duration. The main objective of this article is to improve the speed of power tracking through a dynamic adjustment of the power tracker's sampling time. Although the same idea was already deployed in the literature, existing methodologies are essentially based upon tedious offline assessments of converter dynamics using the PV module information. In contrast, the proposed dynamic moment-based adaptive rate sampling (D-MARS) scheme modulates the sampling time of the power tracking controller by monitoring the actual state of converter dynamics through a moving variance calculation in real time. Detailed experimental studies are performed to verify the benefit of the proposed D-MARS scheme over the other sampling time modulation (STM) techniques.**

***Index Terms*—Converter transient, moving variance, photovoltaic (PV) system, power tracking, sampling time modulation (STM).**

Nomenclature

D-MARS	Dynamic moment-based adaptive rate sampling.
EOP	Equilibrium operating point.
FPPT	Flexible power point tracking.
GMPP	Global maximum power point.
ITC	Iteration time counter.
LPF	Low-pass filter.
MMC	Moving moment calculator.
MPP	Maximum power point.
MPPT	Maximum power point tracking.
OGASE	Oscillation-guided adaptive-step enumeration.
PSC	Partial shading condition.
PTC	Power tracking controller.
PV	Photovoltaic.
SDC	Stabilization duration counter.
STM	Sampling time modulation.
TDC	Transient duration counter.
UIC	Uniform irradiance condition.
VCA	Variance crossover angle.
VDP	Variance drop period.

Manuscript received 10 July 2023; revised 21 October 2023; accepted 17 November 2023. Date of publication 24 November 2023; date of current version 22 December 2023. This work was supported by the Science and Engineering Research Board (SERB), Department of Science and Technology, Government of India, under the Grant CRG/2021/004541. Recommended for publication by Associate Editor Y. Li. *(Corresponding author: Vaskar Sarkar.)*

Vinay Kumar Kolakaluri and Vaskar Sarkar are with the Department of Electrical Engineering, Indian Institute of Technology Hyderabad, Kandi 502284, India (e-mail: ee19resch01005@iith.ac.in; vaskar@ee.iith.ac.in).

Mohammad Nair Aalam is with the Center for Power Electronics Systems, Virginia Tech, Blacksburg, VA 24061 USA (e-mail: nairaalam@vt.edu).

Color versions of one or more figures in this article are available at https://doi.org/10.1109/TPEL.2023.3336389.

Digital Object Identifier 10.1109/TPEL.2023.3336389

I. Introduction

DEVELOPMENT of efficient mechanisms for the power tracking control of a PV array has a great significance to expand the scope of deployment of PV systems for serving consumer loads at different scales and in different applications. Two different types of power tracking, namely MPPT [1], [2], [3], [4], [5], [6] and FPPT [7], [8], [9], [10], [11], [12], [13], can be performed for a PV system. The objective of the MPPT control is to operate the PV array only at the MPP of its power–voltage ($P-V$) curve, whereas, the FPPT control provides users with the flexibility to increase or decrease the PV power output as per the exact requirement of system. Because of the nonmonotonic nature of the $P-V$ curve, it is usually difficult to perform any kind of power tracking with the help of a continuous-time controller. Therefore, the practical PV power tracking is usually carried out by means of a system-interactive optimization via a discrete-time control mechanism. In the case of a two-stage PV system, the duty ratio command to the dc–dc converter is to be optimized [14], [15], whereas, optimization of a voltage reference command is required for a single-stage PV system [16], [17]. Out of several performance measures, the swiftness of power tracking is very important to reduce the loss of solar energy as well as to quickly achieve the generation-load balance for maintaining the system stability. The speed of power tracking becomes a more critical concern when the power tracking is to be performed under the PSC. This is because the power tracking under PSC should either involve an additional task of finding the GMPP zone [18], [19], [20], [21], [22], [23], [24], [25] or take the resort of a metaheuristic optimization algorithm [26], [27], [28], [29], [30], [31], [32]. This may significantly lengthen the power tracking duration. One way to improve the speed of power tracking without hampering its steady-state performance

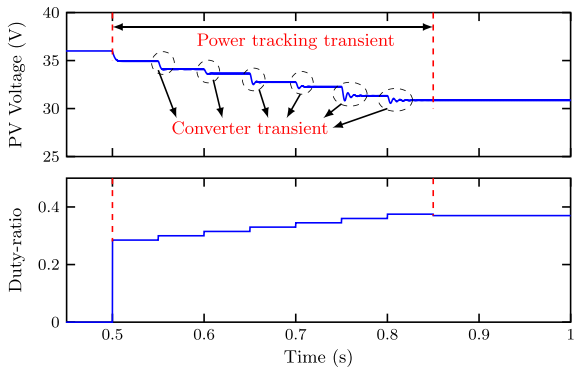

Fig. 1. Illustration of converter transient and power tracking transient.

is to dynamically adjust the size of duty ratio or voltage reference perturbation from one iteration to another iteration of the concerned system-interactive optimization. A large volume of work is available in the literature in this line [2], [3], [4], [5]. It may also be possible to improve the speed of power tracking by dynamically adjusting the PTC sampling time as the power tracking iterations go along.

In a power tracking control algorithm, it is necessary to know the position of the present EOP so as to apply the new duty ratio/voltage reference perturbation in the correct direction. The EOP basically refers to the steady-state PV array output for a specific duty ratio or voltage reference command input to the converter control system. Different types of assessment of the EOP position are carried out by different PTC algorithms. However, there is always a certain time delay to reach the new EOP after making a duty ratio or voltage reference perturbation. The same happens because of the appearance of a converter transient while moving the PV system from one steady state to another steady state. The converter transient phenomenon during the power tracking of a two-stage PV system are illustrated via Fig. 1. It can be seen that there is an exponentially decaying monotonic or sinusoidal variation of the PV array voltage output within the encircled spot after every step of duty ratio perturbations. The respective form of PV voltage variation is essentially caused by the dynamic nature of a converter. In the case the PV array output quantities are sampled during the transient phase of the converter dynamics, there may be a false detection of the corresponding EOP position. Thus, performing power tracking iterations at an arbitrarily high sampling rate may lead to convergence failure in the power tracking result [33], [34], [35]. This, in turn, makes it necessary to tune the PTC sampling time very carefully with due considerations for the settling time of the converter transient.

The settling time of the converter transient depends mainly upon four factors, such as converter parameters, the postperturbation EOP position on the $P-V$ curve, the duty ratio/voltage reference perturbation step size, and the environmental condition [34], [35], [36], [37], [38], [39]. In the traditional MPPT or FPPT control, the power tracking iterations are carried out at fixed sampling intervals [3], [11], [12], [13], [23], [24], [25], [26], [27]. In such a case, the PTC sampling period needs to be adjusted according to the worst-case scenario of converter transients after performing studies over different possible combinations of all the variable factors. However, in a real operating condition, the converter transient may settle down much faster than the worst case scenario. As a result, fixing the PTC sampling time in a conservative manner often adds an extra wait time between two successive power tracking iterations, which, in turn, prolongs the power tracking transient. In order to improve the speed of power tracking, STM techniques were proposed in [39], [40], [41], [42], [43]. The methodology proposed in [39] uses two different sampling times by classifying the duty ratio perturbation step size as large or small. On the other hand, a linear STM rule was proposed in [40], [41], [42], [43] to vary the PTC sampling period as a linear function of the duty ratio perturbation step size. It is, however, to be noted that the STM techniques proposed in [39], [40], [41], [42], and [43] make the PTC sampling time adaptive only to the duty ratio perturbation step size. There is still a requirement to perform extensive offline studies of the converter dynamics for different environmental conditions and postperturbation EOP positions while parameterizing such static STM rules. The module parameters of the PV array also need to be known to formulate the STM function.

The novel contribution of the present article lies in performing the PTC STM with a closer observation of the real-time converter dynamics instead of using any static rule. Thus, the STM is automatically adapted to the postperturbation EOP position or the environmental condition. The proposed sampling time modulator is referred to as a D-MARS controller. Here, the STM decision is actually taken by analyzing the statistical moments, such as mean and variance, of high-frequency measurements collected from the PV array. The D-MARS controller is developed to deliver the following benefits in comparison to the existing techniques.

1) Nondependence on the PV module parameters (i.e., the make of the PV module).
2) Easy parameter tuning
3) Improved speed of power tracking

In addition, the proposed D-MARS controller is designed in a way so that it can be used with any PTC under both uniform irradiance and partial shading. Specific attention is paid to prevent too early or too late generation of the sampling pulse. It is to be noted that such a model-free and purely dynamic way of modulating the sampling time of a PV PTC has still not been reported in the literature. The present work focuses mainly on a two-stage PV system. However, the STM scheme proposed is generic enough to be used with the power tracker of a single-stage PV system as well.

The rest of this article is organized as follows. The block diagram and control logic of the D-MARS controller are thoroughly explained in Section II. In order to provide a visual illustration of the STM functionality of the D-MARS controller, a brief simulation study is performed in Section III. Experimental results are produced in Section IV to justify the benefit of the proposed D-MARS controller over the available static sampling time modulators for different types of power tracking. Finally, Section V concludes this article.

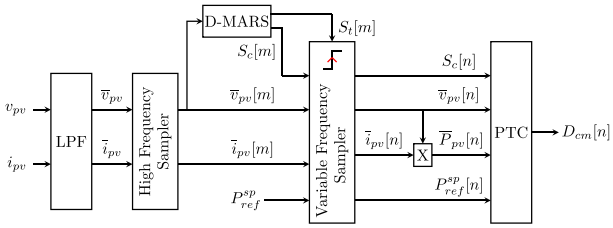

Fig. 2. Layout of the proposed D-MARS assisted PTC.

II. Proposed D-MARS Scheme

The combined arrangement of D-MARS and PTCs is shown by the block diagram in Fig. 2. The PV array voltage and current measurements are initially processed by a LPF to suppress unwanted ripples because of noise and other factors. The filtered current and voltage measurements are indicated by $\overline{v}_{\rm pv}$ and $\overline{i}_{\rm pv}$, respectively. The D-MARS controller uses a high-frequency sampler to collect the voltage measurement from the LPF output. The current measurement can also be collected along with the voltage measurement through the same high-frequency sampler. The high-frequency voltage and current samples are then resampled by a variable-frequency sampler for being used by the PTC. Another input to the PTC is the power reference command in the case of the FPPT. The sampling instants of the high-frequency and variable-frequency samplers are indicated by m and n, respectively. The D-MARS controller plays the role of modulating the sampling rate of the variable-frequency sampler. The noise-free high-frequency voltage samples obtained at the output of the high-frequency sampler are directly used by the D-MARS controller. By using the above mentioned high-frequency voltage samples, the D-MARS controller performs a statistical moment analysis to evaluate the state of the converter dynamics. Two binary outputs (i.e., S_t and S_c) are produced by the D-MARS controller. The variable-frequency sampler collects a new set of samples and initiates the next power tracking iteration only after seeing a rising edge in S_t. Under the normal condition, the S_t signal remains low as long as the converter dynamics is in the transient phase. The status of S_t should be changed to the high value only after the converter transient subsides significantly. There are, however, instances in which the converter transient sustains for a very long time duration. The particular situation typically arises if the converter transient has to be settled in a positive slope region of the $P-V$ curve [18], [38]. Under such a situation, signal S_t is prematurely raised to the high value even though the converter transient is still ongoing. The value of S_c is, as well, set to one, indicating the premature generation of the triggering pulse to the variable-frequency sampler. Signal S_c is also passed to the PTC to be used for the horizontal position detection of the present EOP. If S_c is zero, the normal logic is followed to determine whether the present EOP is on the left or right side of the power peak of a hill. Otherwise, it is directly inferred that the power tracking trajectory is still on the left side of the corresponding power peak. The final output of the PTC is a duty ratio command, which is passed to the dc–dc converter switches to take the power tracking trajectory to a new EOP.

A. Internal Block Diagram of D-MARS Controller

The internal block diagram representation of the D-MARS controller is shown in Fig. 3. The external input to the D-MARS controller is marked by a red circle, and its final outputs are indicated by red squares. The main building blocks of the D-MARS controller are a MMC, a SDC, a TDC, and an ITC. The output of a z^{-1} block is the one time-step delayed value of its input signal. On the other hand, the output of a $\widehat{\mathbf{z}}^{-k}$ block is a vector of $(k+1)$ most recently collected samples including the present one. The MMC block computes the mean (i.e., μ_v) and variance (i.e., σ_v) of voltage samples obtained through a moving time-window. Essentially, the most recent M samples of the PV array voltage are used to perform the aforementioned mean and variance calculation, where M is given by

$$M = \frac{T_W}{T_s^{\rm hf}}. \tag{1}$$

In (1), symbol T_W stands for the moving time-window length, and $T_s^{\rm hf}$ is the sampling period of the D-MARS controller. It is to be noted that T_W should be an integer multiple of $T_s^{\rm hf}$. As the converter transient notably subsides, the PV array voltage becomes almost constant; hence, its moving variance periodically drops below a certain threshold line. It is, however, necessary to see the persistence of the above mentioned variance drop for a minimum time duration to make a credible inference about the subsidence of the converter transient. Therefore, an SDC block is employed to monitor the time period of the particular variance drop condition. The TDC is responsible for keeping track of the time elapsed since the last duty ratio perturbation. The necessity of the TDC arises in order to deal with the case of prolonged converter transient. Finally, the objective of the ITC is to count the time since the beginning of the new power tracking iteration after obtaining an S_t pulse.

There are comparator blocks in the D-MARS controller to take certain actions based upon the counter outputs. Once the SDC or TDC output exceeds a threshold value, the state of the sampler trigger signal S_t is changed from zero to one in the next time instant. Crossing of the TDC threshold also sets the sampling counter flag S_c to one. The ITC output is actually used to reset the SDC and TDC outputs after completing one power tracking iteration. The completion of each power tracking iteration essentially indicates the beginning of a new era of converter transients because of introducing another duty ratio perturbation. As the ITC output exceeds the threshold value set for it, the reset signal $R_{\rm st}$ for SDC and TDC is immediately raised to one. The threshold values of counter outputs (i.e., $C_{\rm sb,cr}$, $C_{\rm tr,cr}$, and $C_{\rm pt,cr}$) are obtained via the following equations:

$$C_{\rm sb,cr} = \frac{T_{\rm sb,min}}{T_s^{\rm hf}} \tag{2}$$

$$C_{\rm tr,cr} = \frac{T_{\rm tr,max}}{T_s^{\rm hf}} \tag{3}$$

$$C_{\rm pt,cr} = \frac{T_{\rm pti}}{T_s^{\rm hf}}. \tag{4}$$

Here, $T_{\rm sb,min}$ is the lower limit on the VDP for the purpose of indicating converter transient stabilization. The upper limit on

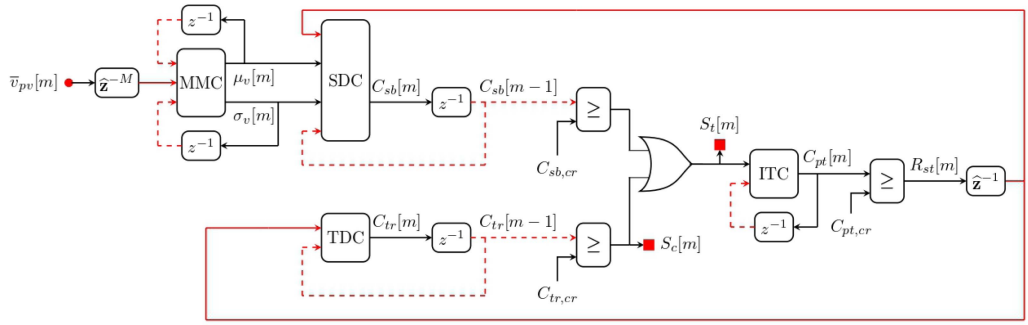

Fig. 3. Internal block diagram of the D-MARS controller.

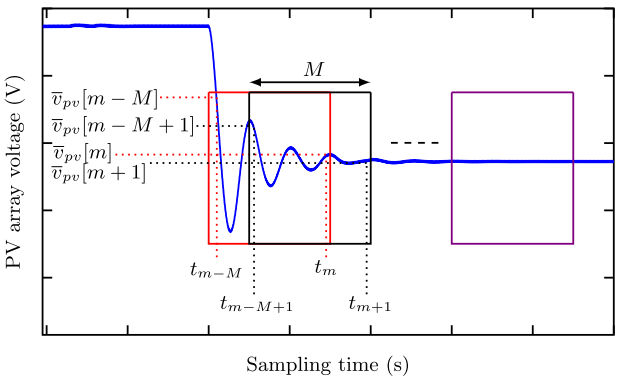

Fig. 4. Illustration of moving variance concept.

the PTC sampling time interval is indicated by $T_{\text{tr,max}}$, whereas, T_{pti} is the maximum time required to complete one power tracking iteration. The sequence of execution of different blocks of the D-MARS controller is decided by the solid arrows in Fig. 3.

B. Dynamics of D-MARS Building Blocks

The general functionality of different blocks of the D-MARS controller is explained in the previous section. The present section speaks about the specific logic that is followed to implement each block. As the dynamics of a discrete-time system is usually represented by means of difference equations, the same format is employed to explain the computation of a block output at every time instant. The initial values of all the state variables of the D-MARS controller should be set to zero.

1) MMC: As mentioned earlier, the specific statistical moments that are of interest here are the mean and variance of PV array voltage samples that are acquired through a sliding time-window. The concept of the sliding time-window is illustrated via Fig. 4. The red and black rectangular boxes indicate the sliding window positions at mth and $(m+1)$th time instants, respectively. The objective of using a sliding time-window is to look only into a small segment of the voltage variation curve so as to limit the data size as well as to avoid the interference of the transient section in the detection of the converter steady state. Thus, once the time-window moves to the position of the purple rectangular box, a steady output of the PV array becomes very apparent.

The moving mean and variance of voltage samples at the mth time instant are given by the following equations:

$$\mu_v[m] = \frac{\sum_{j=1}^{M} v_{\text{pv}}[m-M+j]}{M} \tag{5}$$

$$\sigma_v[m] = \frac{\sum_{j=1}^{M} (v_{\text{pv}}[m-M+j] - \mu_v[m])^2}{M}. \tag{6}$$

It is, however, difficult to implement (5) and (6) in a microcontroller because of its very limited computational capability. Therefore, it is more appropriate to use the following recursive formulae for the moving mean and variance calculation:

$$\mu_v[m] = \mu_v[m-1] + \left(\frac{v_{\text{pv}}[m] - v_{\text{pv}}[m-M]}{M}\right) \tag{7}$$

$$\begin{aligned}\sigma_v[m] = \sigma_v[m-1] &+ \left(\frac{v_{\text{pv}}[m] - v_{\text{pv}}[m-M]}{M}\right) \\ &\times \left\{\left(\frac{M+1}{M}\right) v_{\text{pv}}[m] - 2\mu_v[m] \right. \\ &\left. + \left(\frac{M-1}{M}\right) v_{\text{pv}}[m-M]\right\}. \end{aligned} \tag{8}$$

Detailed derivations of (7) and (8) can be found in [44]. The self-feedback inputs to the MMC block in Fig. 3 provide the information of $\mu_v[m-1]$ and $\sigma_v[m-1]$. It is to be noted that the use of the recursive formulae also requires the information of the last sample (i.e., $v_{\text{pv}}[m-M]$) in the previous time window. Hence, the input vector to the MMC block is assigned to contain $(M+1)$ most recent voltage samples instead of only M samples.

2) ITC: The ITC is reset to zero after observing a rising edge in S_t. Otherwise, it keeps incrementing its count by one at every time instant. Thus, the dynamics of the ITC block can be mathematically described as follows:

$$\begin{aligned} C_{\text{pt}}[m] &= 0, \text{ if } S_t[m] \neq S_t[m-1] = 1 \\ &= C_{\text{pt}}[m-1] + 1, \text{ otherwise.} \end{aligned} \tag{9}$$

It is also possible to saturate the ITC output to an upper limit once it exceeds $C_{\text{pt,cr}}$.

3) SDC: As mentioned earlier, the objective of SDC is to compare σ_v with a certain threshold value. Let the threshold value of σ_v be indicated by $\sigma_{v,\text{cr}}$. The following equation is used to derive $\sigma_{v,\text{cr}}$:

$$\sigma_{v,\text{cr}}[m] = \{\varepsilon_{\text{cr}}\mu_v[m]\}^2 . \tag{10}$$

The critical variability fraction parameter (i.e., ε_{cr}) needs to be designed by the user. The SDC starts counting time when σ_v falls below the $\sigma_{v,\text{cr}}$-line. The counting halts and the SDC output comes back to zero if either σ_v again rises above the $\sigma_{v,\text{cr}}$-line or a rising edge happens in the ITC comparator output. Thus, the following equation governs the SDC dynamics:

$$\begin{aligned} C_{\text{sb}}[m] &= 0, \text{ if } \sigma_v[m] > \sigma_{v,\text{cr}}[m] \\ &= 0, \text{ if } R_{\text{st}}[m] \neq R_{\text{st}}[m-1] = 1 \\ &= C_{\text{sb}}[m-1] + 1, \text{ otherwise.} \end{aligned} \tag{11}$$

The output of the SDC block usually remains pulsating during the converter transient.

4) TDC: The dynamics of the TDC block is shown through the following equation:

$$\begin{aligned} C_{\text{tr}}[m] &= 0, \text{ if } R_{\text{st}}[m] \neq R_{\text{st}}[m-1] = 1 \\ &= C_{\text{tr}}[m-1] + 1, \text{ otherwise.} \end{aligned} \tag{12}$$

The TDC is reset to zero when a rising edge is observed in the output of the ITC comparator. On any other occasion, the TDC keeps counting the time instants normally. The TDC output can also be saturated to an upper limit.

C. D-MARS Controller Parameter Design

It is necessary to find out the values of T_s^{hf}, T_{pti}, ε_{cr}, $T_{\text{tr,max}}$, T_W, and $T_{\text{sb,min}}$ before using the D-MARS controller for the PTC STM. Out of these six parameters, the first two are inherent features of the power conversion system. Therefore, the respective parameters are actually to be estimated instead of being designed. The sampling period T_s^{hf} of the D-MARS controller essentially indicates the maximum execution time of its one iteration. The particular value can be easily determined by monitoring the clock time reported by the microcontroller board at the end of each D-MARS iteration. In the same way, the value of T_{pti} can be directly obtained by monitoring the execution times of individual power tracking iterations.

Unlike T_s^{hf} and T_{pti}, the other parameters are related to the efficient functioning of the D-MARS controller. Therefore, the particular parameters should be designed in a way so that the STM is optimized. The D-MARS controller parameter tuning needs the information of only the converter parameters and the PV array ratings. As mentioned earlier, no specific details of the constituent modules of the PV array are required. In subsequent sections, symbols L_{dc} and C_{pv} will be used to indicate the inductance and input capacitance, respectively, of the dc–dc converter that interfaces the PV array with a voltage controlled dc bus. The MPP voltage and MPP current corresponding to the standard test condition are indicated by $v_{\text{pv,stc}}^{\text{mpp}}$ and $i_{\text{pv,stc}}^{\text{mpp}}$, respectively. The critical variability fraction (i.e., ε_{cr}) or the upper limit on the PTC sampling interval (i.e., $T_{\text{tr,max}}$) is to be designed separately. On the other hand, the moving window length and the VDP lower limit (i.e., T_W and $T_{\text{sb,min}}$) are to be jointly optimized.

1) Designing ε_{cr}: In principle, the value of ε_{cr} should be as small as possible. However, an infinitesimally small ε_{cr} value may make the threshold variance line practically unreachable because of the presence of some residual ripples in measurements despite low-pass filtering. In order to deal with the particular situation, the value of ε_{cr} may be set equal to the normalized width of the experimentally observed ripple band with respect to the mean voltage in a steady state.

2) Designing $T_{tr,max}$: As mentioned earlier, the issue of imposing an upper limit on the PTC sampling interval arises because of the prolonged power tracking transient in the positive-slope region of the $P-V$ curve. Thus, $T_{\text{tr,max}}$ may be chosen according to the small-signal settling time of the converter transient at an MPP. The small-signal settling time around any EOP, however, depends upon the incremental conductance of the PV array at the respective EOP [35]. It can, further, be shown that the incremental conductance of the PV array at an MPP is always equal to the ratio of the corresponding current and voltage with a negative sign [45]. As the MPP current decreases or the MPP voltage increases, the associated incremental conductance magnitude also decreases, leading to in a higher settling time of the converter transient. By assuming UIC, the MPP voltage exhibits very little variation with the irradiance, whereas, the MPP current varies almost proportionally. This, in turn, makes the MPP incremental conductance inversely proportional to the irradiance under UIC. Therefore, the MPP under the lowest possible uniform irradiance can be chosen as the reference MPP to represent the worst case scenario for designing $T_{\text{tr,max}}$. It is also to be noted that the magnitude of incremental conductance at an MPP under the PSC is usually higher than the magnitude of MPP incremental conductance under the lowest possible uniform irradiance. According to the settling time formula presented in [35], [37], the expression of $T_{\text{tr,max}}$, thus, appears as follows:

$$T_{\text{tr,max}} = 6\left(\frac{C_{\text{pv}}}{E_{\text{min}}}\right)\left(\frac{v_{\text{pv,stc}}^{\text{mpp}}}{i_{\text{pv,stc}}^{\text{mpp}}}\right). \tag{13}$$

Here, E_{min} refers to the minimum irradiance (in kW/m^2) under which the PV array is expected to operate. All other symbols have already been explained in the previous paragraph. In the present article, the value of E_{min} is taken to be 0.1 kW/m^2. Factor "6" in (13) has been found by considering a 5% tolerance band that should be sufficient to indicate the end of a small-perturbation transient.

3) Designing T_W and $T_{sb,min}$: The observation time-window length and the VDP lower limit are designed on the basis of a moving variance analysis of the following vertically shifted sinusoidal function.

$$x = x_b\left(1 + h_p \sin\delta\right). \tag{14}$$

In (14), quantities x_b and h_p are independent of δ. The moving average and variance of the above signal are evaluated in the continuous domain for an observation window of $\Delta\theta_W$ radian. If the angular position of the left edge of the observation window

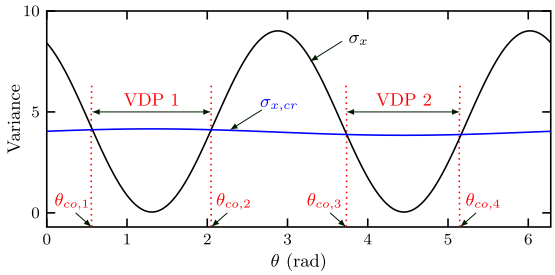

Fig. 5. Illustration of VDP and VCA.

is θ, the moving average and variance of signal x can be found as follows:

$$\mu_x(\theta) = \frac{1}{\Delta\theta_W}\int_{\theta}^{\theta+\Delta\theta_W} x\,d\delta \tag{15}$$

$$\sigma_x(\theta) = \frac{1}{\Delta\theta_W}\int_{\theta}^{\theta+\Delta\theta_W} \{x-\mu_x(\theta)\}^2\,d\delta. \tag{16}$$

It is easy to perform the integrations in (15) and (16). A plot of $\sigma_x(\theta)$ together with the plot of $\sigma_{x,\mathrm{cr}}(\theta)$ as per (10) is presented in Fig. 5. It can be seen that σ_x drops below $\sigma_{x,\mathrm{cr}}$ two times within $0 \le \theta \le 2\pi$. The corresponding VDPs are enclosed by dotted red lines in Fig. 5. The same pattern is repeated in the subsequent periods of x. Angles $\theta_{\mathrm{co},1}$, $\theta_{\mathrm{co},2}$, $\theta_{\mathrm{co},3}$, and $\theta_{\mathrm{co},4}$ are referred to as VCAs. The VCAs are essentially the solutions of the following equation:

$$\sigma_x(\theta) = \{\varepsilon_{\mathrm{cr}}\mu_x(\theta)\}^2. \tag{17}$$

Equation (17) involves only a single variable; therefore, its all the solutions can be found simply by enumerating over θ with a very small incremental step size. Each VDP is defined by a VCA with rising variance and its preceding VCA with falling variance. Out of the two VDPs in Fig. 5, the longer one (i.e., with larger angular span) is considered as the critical VDP. Let the angular length of the critical VDP be indicated by $\Delta\theta_{D,\mathrm{cr}}$. The value of $\Delta\theta_{D,\mathrm{cr}}$ depends upon $\Delta\theta_W$ and h_p. However, it can be easily proven that x_b in (14) has no effect on $\Delta\theta_{D,\mathrm{cr}}$.

In order to proceed further toward the D-MARS controller parameter tuning, it is important to study the effects of $\Delta\theta_W$ and h_p on the combined angular span of the observation window and the critical VDP. The particular angular quantity is symbolized as $\Delta\theta_{\mathrm{DW}}$. That is

$$\Delta\theta_{\mathrm{DW}} = \Delta\theta_{D,\mathrm{cr}} + \Delta\theta_W. \tag{18}$$

The variation of $\Delta\theta_{\mathrm{DW}}$ with h_p for different values of $\Delta\theta_W$ is shown in Fig. 6(a), whereas, Fig. 6(b) shows that variation of $\Delta\theta_{\mathrm{DW}}$ with $\Delta\theta_W$ by keeping h_p as a parameter. From Fig. 6, it is apparent that angle $\Delta\theta_{\mathrm{DW}}$ is a decreasing function of h_p. In other words, for a given length of the observation window, the critical VDP angle either becomes smaller or remains unchanged as h_p increases. In contrast, the sensitivity of $\Delta\theta_{\mathrm{DW}}$ to $\Delta\theta_W$ can be both positive and negative. This, in turn, produces a minima in each plot of Fig. 6(b).

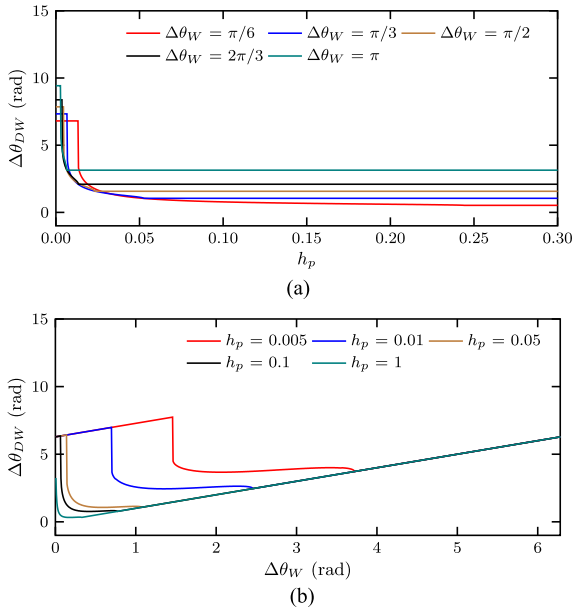

Fig. 6. Variation of $\Delta\theta_{\mathrm{DW}}$. (a) With respect to h_p. (b) With respect to $\Delta\theta_W$.

The analysis performed above is relevant to the D-MARS controller parameter design, since the converter transient following a duty ratio perturbation exhibits a damped sinusoidal variation. An exponentially decaying sinusoidal function can be approximated as a sequence of pure sinusoids with stepped amplitude variations. Thus, signal x in (14) approximates of the variation of the PV array voltage during each oscillation period with the steady-state voltage being indicated by x_b. Moreover, the mean and variance calculated in the continuous domain may be closely approximated by discrete-domain calculations with a high sampling frequency. The value of the overshoot fraction h_p gradually declines from one time period to another time period. The end of the converter transient can be declared when h_p becomes sufficiently small. It may, however, be difficult to directly determine h_p in real-time. Therefore, the threshold value of h_p to mark the subsidence of the converter transient should alternatively be modeled via a lower limit on the VDP. For the chosen threshold value of h_p, the optimal observation window and limiting VDP lengths in angular terms are given by the corresponding minima in 6(b). As a larger observation window length increases the time delay to recognize a duty ratio perturbation, and a higher VDP limit increases the delay in concluding transient subsidence, it is appropriate to minimize the sum of both quantities so as to make the power tracking faster. The angular values of the observation window and the VDP limit are to be converted into time values based upon the frequency of the PV voltage oscillation. Since the oscillatory frequency of the PV voltage is almost equal to the natural frequency of the dc–dc converter, the following equations can be used to convert an angle into the time quantity.

$$T_W = T_s^{\mathrm{hf}} \times \mathrm{round}\left(\frac{\theta_W^* \sqrt{L_{\mathrm{dc}}C_{\mathrm{pv}}}}{T_s^{\mathrm{hf}}}\right) \tag{19}$$

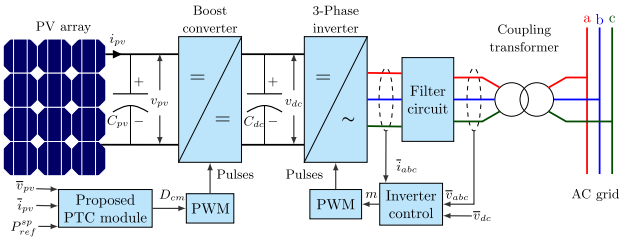

Fig. 7. Schematic diagram of two-stage grid-connected PV system.

TABLE I
DC-SIDE SPECIFICATIONS OF THE TWO-STAGE PV SYSTEM

Parameter	Value
PV array open circuit voltage, short circuit current, MPP voltage, and MPP current under the standard test condition	36 V, 3 A, 90 W, 31 V, 2.9 A
Boost converter inductance, input capacitance, output capacitance, maximum duty ratio	2.5 mH, 0.47 mF, 1 mF, 0.65
DC-link reference voltage	48 V
Boost converter switching frequency, LPF cut-off frequency	10 kHz, 1 KHz
PWM and D-MARS sampling periods	1 μs, 0.45 ms
D-MARS parameters T_W, ε_{cr}, $T_{sb,min}$, $T_{tr,max}$, and T_{pti}	3.6 ms, 0.004, 0.88 ms, 0.3 s, 5.4 ms

$$T_{\text{sb,min}} = \theta^{*}_{D,\text{cr}}\sqrt{L_{\text{dc}}C_{\text{pv}}}. \tag{20}$$

The asterisks in superscripts indicate optimal values of corresponding quantities for the chosen threshold value of h_p. In the present article, the threshold value of h_p is taken as 1% or 0.01. It is to be noted that, unlike the settling time calculation, the percentage number used here is basically related to the final PV array voltage rather than its incremental variation.

III. ILLUSTRATION OF THE STM WITH THE PROPOSED D-MARS CONTROLLER

In order to clearly explain the working of the proposed D-MARS assisted power tracking control, a simulation study is performed on a two-stage grid-connected PV system. The schematic diagram of the PV system considered is shown in Fig. 7. The dc-side plant and controller parameter data is provided in the Table I. The PV array is assumed to be operating under partial shading, and a simulation for power tracking under the same condition is performed. The $P-V$ curve under the given partial shading scenario is shown in Fig. 8. The D-MARS controller is deployed along with the MPPT controller proposed in [27]. The simulation results for the PV array voltage, moving variance of the PV array voltage, D-MARS trigger signal, and the dc–dc converter duty-ratio are shown in Fig. 9. The variable sampling time is visible from different time durations of the steps in the duty ratio waveform. When a duty-ratio perturbation is applied, the moving variance of the PV array voltage increases sharply. As the converter transient comes to an end, the particular variance value decreases almost to zero. This can be observed in Fig. 9. As the moving variance continuously remains at a very low value, the SDC block of the D-MARS controller releases a sampling pulse triggering the next power tracking iteration. There are, however, some instances at which the moving variance of the

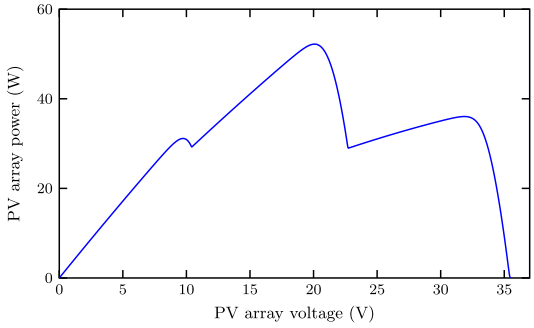

Fig. 8. $P-V$ curve used for the demonstration of the proposed D-MARS functionality.

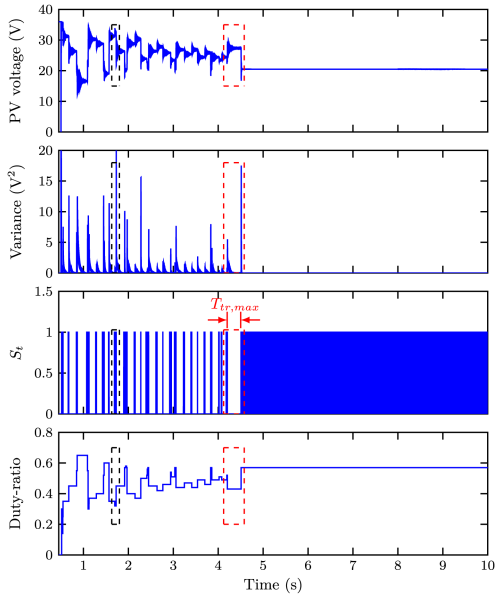

Fig. 9. Simulation results for the D-MARS assisted MPPT control under PSC.

PV array voltage falls below $\sigma_{v,\text{cr}}$, but rises again within a short while. One such instance can be observed inside the dashed black rectangular box marked on each subplot of Fig. 9. A zoomed view of this particular scenario (i.e., from 1.695 s to 1.73 s) is shown in Fig. 10. From Fig. 10, it is clearly visible that, at $t = 1.7235$ s, the moving variance of PV array voltage shows a momentary dip below $\sigma_{v,\text{cr}}$. Although SDC was started, it could not complete the count; hence no sampling trigger is generated. Again, the moving variance of PV array voltage falls below $\sigma_{v,\text{cr}}$ at $t = 1.7265$ s and continues to be below $\sigma_{v,\text{cr}}$ till $t = 1.7274$ s. As the moving variance of PV array voltage remains lower than $\sigma_{v,\text{cr}}$ for more than 0.88 ms (i.e., $T_{\text{sb,min}}$), signal S_t becomes high owing to the SDC.

In the case of a prolonged converter transient during the power tracking process, the moving variance of PV array voltage fails to remain below $\sigma_{v,\text{cr}}$ for a sufficient duration. The dashed red rectangular box indicates one such instance in Fig. 9. A zoomed view of this particular time window (i.e., from 4.19 s to 4.52 s) is shown in Fig. 11. From Fig. 11, it can be observed that the moving variance of PV array voltage from $t = 4.2026$ s

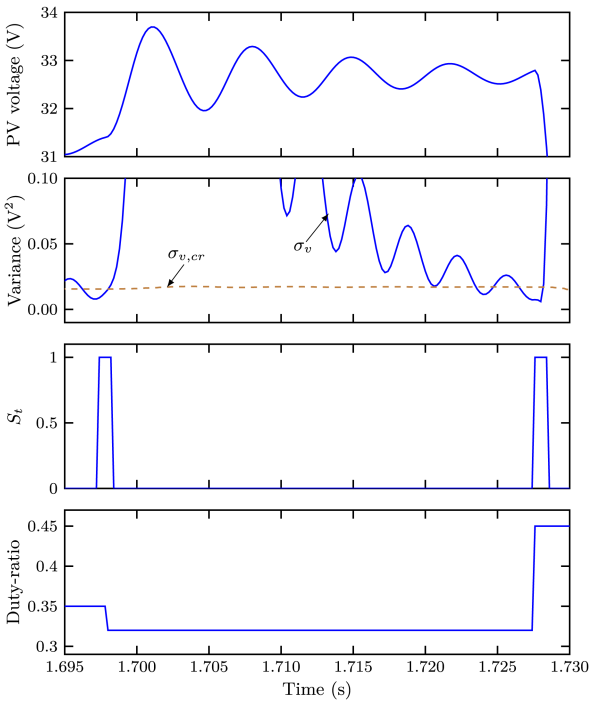

Fig. 10. Zoomed view of dashed black rectangular box of Fig. 9.

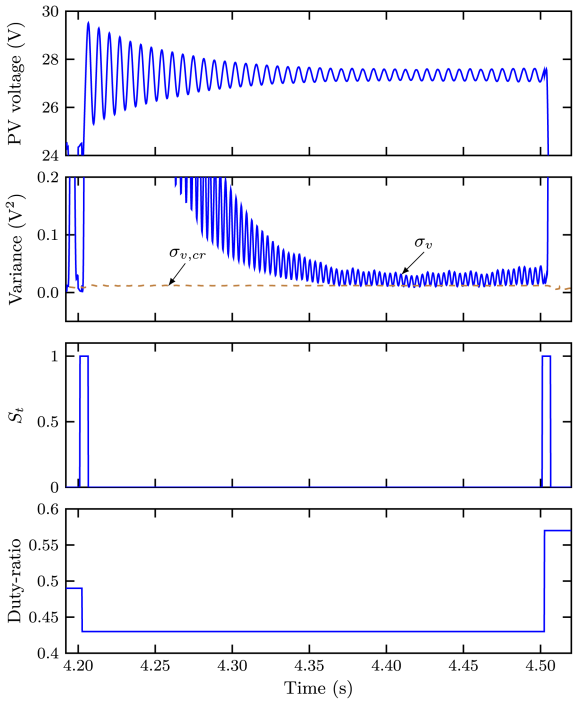

Fig. 11. Zoomed view of dashed red rectangular box of Fig. 9.

to $t = 4.5026$ s never stays below the $\sigma_{v,\mathrm{cr}}$ line continuously for 0.88 ms. As a consequence, the SDC could not trigger the sampling pulse. Thus, the maximum wait time (i.e., 0.3 s) permitted by the TDC is hit or violated. This, in turn, causes TDC to fire the sampling pulse at $t = 4.5026$ s.

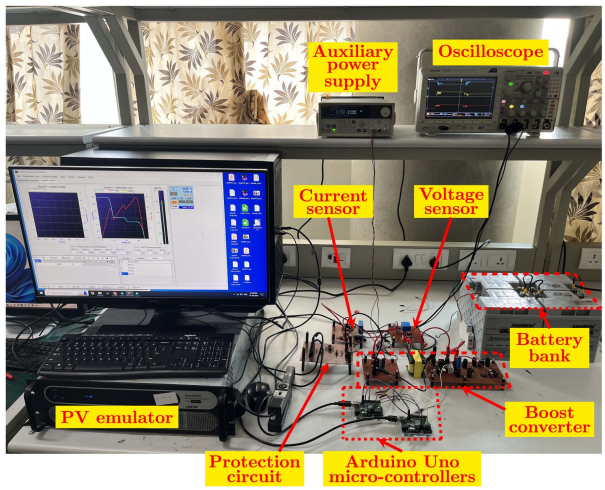

Fig. 12. Photograph of the experimental setup.

TABLE II
STM RULES FOR THE APPLICATION OF EXISTING VARIABLE SAMPLING TIME SCHEMES

Approach	STM rule
Variable sampling proposed in [39]	$\begin{cases} 0.3\text{ s}, & \text{if } \Delta D \geq 0.03 \\ 0.2\text{ s}, & \text{otherwise.} \end{cases}$
Variable sampling proposed in [40]–[42]	$14.96\Delta D + 188.27$

IV. EXPERIMENTAL VERIFICATION

An experimental study is performed to show the practical implementability of the proposed D-MARS approach for performing the MPPT/FPPT control. The usefulness of the D-MARS scheme is also verified by comparing its performance with the performance of existing STM techniques. The main power tracking is performed by using the MPPT/FPPT control algorithms available in the literature, but results are produced by varying the sampling time in different ways. In the experimental setup, the voltage controlled dc-link capacitor is represented by means of a simple dc voltage source so as to avoid the complexity of grid synchronization. A photograph of the experimental setup is shown in Fig. 12. An AMETEK-ETS600X solar PV emulator is used to mimic the characteristics of the PV array under various environmental conditions. The PV array voltage and current are measured by using LEM voltage (LV 25-P) and current (LA 25-P) sensors. An Arduino Uno microcontroller board is used for the real-time implementation of the variable sampling time power tracking control. The LPF is implemented in another Arduino Uno microcontroller board. The LPF output is transferred to the power tracking control system in the other microcontroller board by means of the I^2C communication. The same PV array and D-MARS controller of Table I are used once again. The STM rules followed for the implementation of existing approaches are summarized in Table II. Here, ΔD indicates the duty ratio perturbation step size. The static STM parameter values reported in Table II seem to significantly differ from the respective values in original papers. There are two reasons behind having this difference.

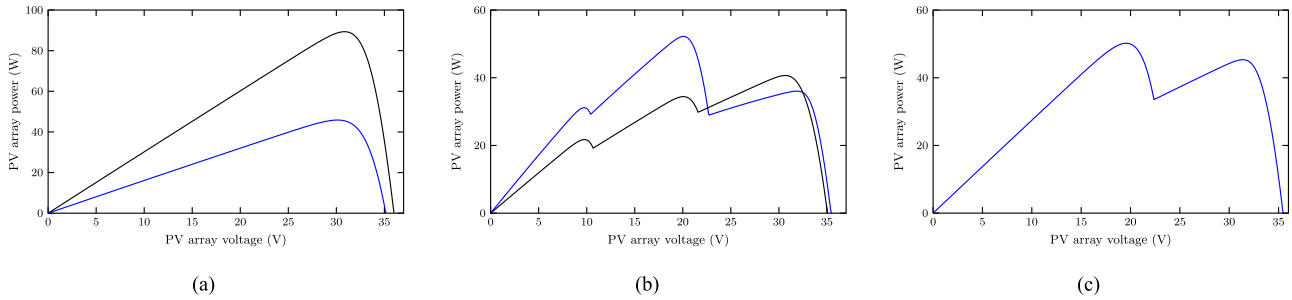

Fig. 13. $P-V$ curves for different power tracking control studies by hardware experimentation. (a) MPPT and FPPT control under UIC. (b) MPPT control under PSC. (c) FPPT control under PSC.

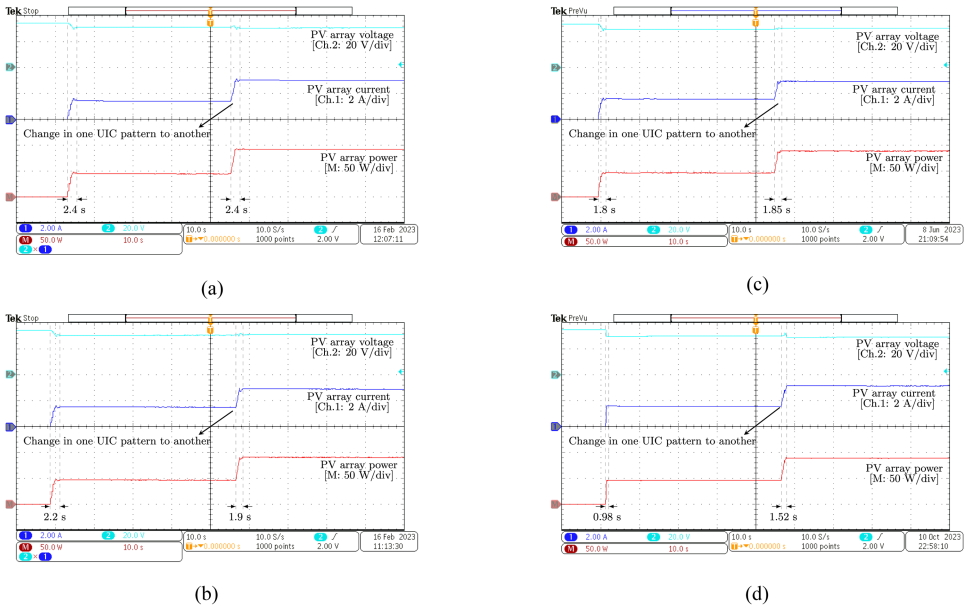

Fig. 14. Experimental results for the MPPT control under UIC. (a) Fixed sampling time approach. (b) Variable sampling time approach proposed in [39]. (c) Variable sampling time approach proposed in [40], [41], [42]. (d) D-MARS scheme.

1) The test system used in the present article is different from the earlier test systems.
2) In order to successfully deploy the existing STM methodologies in the case studies of the present paper, the associated parameters had to be tuned in a more conservative manner by considering a larger set of environmental conditions and postperturbation EOP positions.

Apart from using variable sampling time, results are also produced for the classical fixed sampling time approach. In the case of the fixed rate sampling, the sampling time is set to 300 ms as per the worst case scenario of the variable sampling time approach of [39]. The different $P-V$ curves used to perform the experimental studies are shown in Fig. 13. Four different cases are studied considering both the UIC and partial shading. In each case, the PV array remains in the open circuited condition for some time until the microcontroller is turned ON and pulses are applied to the converter switches. After the system starts running and the steady state for the initial operating condition is attained, a new power tracking round is triggered by changing the operating condition itself. Both the start-up and run-time transients are shown in the results. The PV array voltage, current, and power waveforms are captured in the oscilloscope. These are indicated by the green, blue, and red curves, respectively, in different plots.

A. *Case 1: MPPT Control Under Uniform Irradiance*

In this case, the PV array is initially exposed to an irradiance of 0.5 kW/m^2. Subsequently, the irradiance value is increased to 1 kW/m^2 in a stepped manner. The corresponding $P-V$ curves are shown in Fig. 13(a). The OGASE controller proposed in [11] is used to perform the power tracking. Although the OGASE controller was originally devised to perform FPPT, it can as well be configured as an MPPT controller by setting the power reference command to a very high value. Results for this case with different sampling time modulators are presented in Fig. 14.

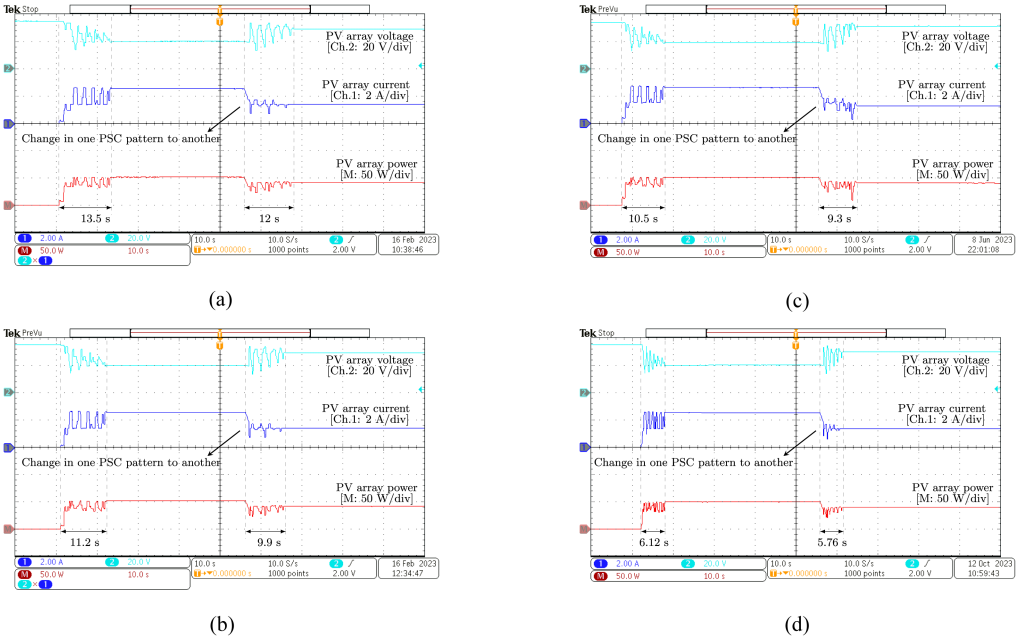

Fig. 15. Experimental results for the MPPT control under PSC. (a) Fixed sampling time approach. (b) Variable sampling time approach proposed in [39]. (c) Variable sampling time approach proposed in [40], [41], [42]. (d) D-MARS scheme.

B. Case 2: MPPT Control Under Partial Shading

The MPPT control under PSC is carried out by using the adaptive velocity particle swarm optimization algorithm proposed in [27]. The $P-V$ curves used for this particular study are shown in Fig. 13(b). Initially, the PTC tracks the MPP on the blue-colored $P-V$ curve in Fig. 13(b). Later, the $P-V$ curve is changed to the black-colored one with a lower global peak. The experimental results for this case are produced in Fig. 15.

C. Case 3: FPPT Control Under Uniform Irradiance

The FPPT control under UIC is performed by using the same OGASE controller as was used in Case 1. To test the FPPT operation, the irradiance pattern is kept constant, but the power reference command is varied. Initially, the power reference command is set to 100 W and, then, reduced to 70 W. The $P-V$ curve depicted with black color in Fig. 13(a) is used to perform the experiment for this test scenario. Fig. 16 presents the results obtained for this particular case.

D. Case 4: FPPT Control Under Partial Shading

In order to perform the FPPT control under the PSC, the multimodality processing adapter proposed in [23] is used along with the OGASE controller. The $P-V$ curve used in this case is shown in Fig. 13(c). For the sake of simplicity in exploring the GMPP zone, only two peaks are considered on the $P-V$ curve. The power reference command is initially set to 30 W. Later, the same is increased to 60 W. Experimental results for the FPPT control under PSC are shown in Fig. 17.

E. Discussion

In order to compare the performances of different PTC STM schemes, the power tracking time for each EOP transition is monitored. The power tracking transient period during an EOP transition is enclosed by a couple of dashed black parallel lines in each oscilloscope plot. The ripples observed outside this particular window basically correspond to the measurement noise. In order to obtain the precise value of the power tracking time, an extra timer is kept inside the PTC code. The particular timer starts counting the time when a new power tracking round begins. After the power tracking converges to the target EOP, the timer count stops, and time counted is transferred to the host computer by the microcontroller via its serial port. A side-by-side comparison of the power tracking time requirements with different PTC sampling time schemes is presented in Table III. The benefit of using variable sampling time is apparent from the table. Among the existing methods, the linear STM scheme proposed in [40], [41], [42] outperforms the discrete STM scheme of [39] in all the cases. This is because the former makes a more precise consideration of both the $P-V$ characteristics of the PV array and the converter parameters. However, the linear STM parameters are not tuned to deal with each environmental condition separately. Instead, the tuning of the linear STM parameters is usually performed by considering the worst case scenario of the environmental condition. On the other hand, the D-MARS controller always responds according to the prevailing environmental condition, since it directly monitors the converter transient in real time. This automatically makes the D-MARS response adaptive to the environmental condition, resulting in faster power tracking. In addition, coefficients of the linear STM equation are obtained by studying only the UICs. Therefore, the

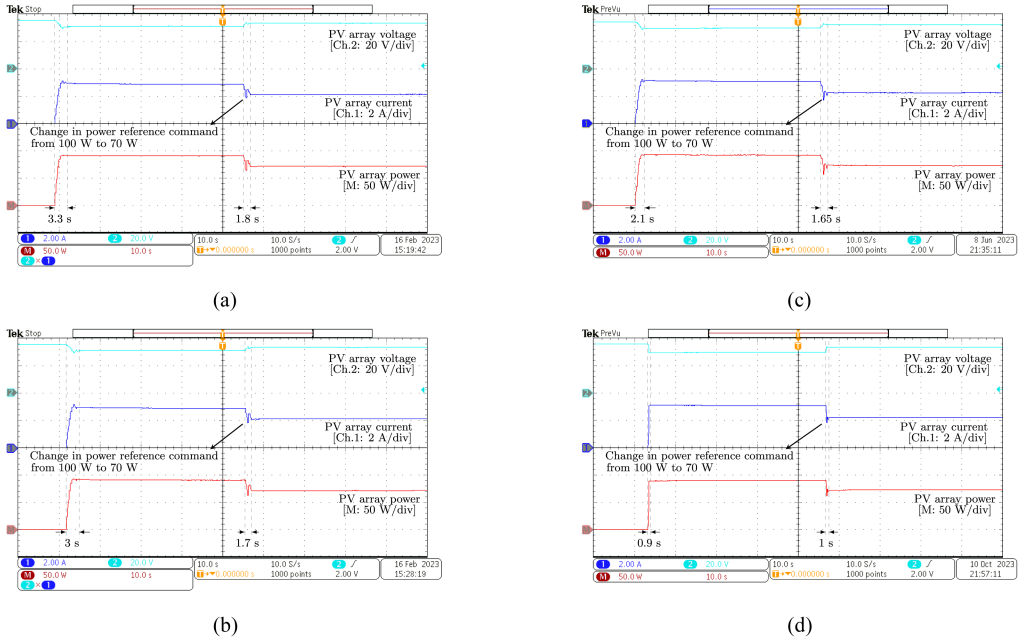

Fig. 16. Experimental results for the FPPT control under UIC. (a) Fixed sampling time approach. (b) Variable sampling time approach proposed in [39]. (c) Variable sampling time approach proposed in [40], [41], [42]. (d) D-MARS scheme.

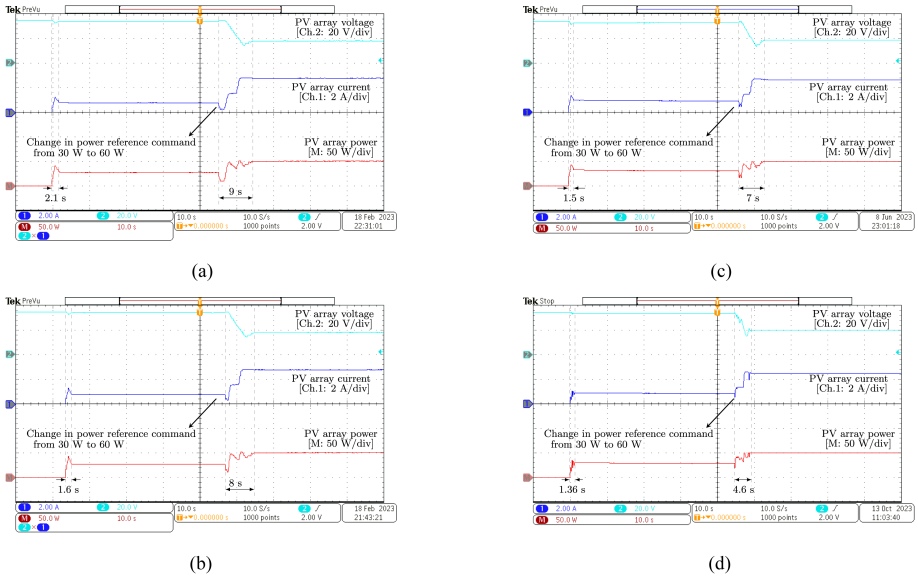

Fig. 17. Experimental results for the FPPT control under PSC. (a) Fixed sampling time approach. (b) Variable sampling time approach proposed in [39]. (c) Variable sampling time approach proposed in [40], [41], [42]. (d) D-MARS scheme.

TABLE III
POWER TRACKING TIME COMPARISON AMONG DIFFERENT PTC STM SCHEMES

PTC mode	Environmental scenario	Fixed sampling		Variable sampling proposed in [39]		Variable sampling proposed in [40]–[42]		D-MARS	
		T-1*	T-2*	T-1*	T-2*	T-1*	T-2*	T-1*	T-2*
MPPT	UIC	2.4 s	2.4 s	2.2 s	1.9 s	1.8 s	1.85 s	0.98 s	1.52 s
	PSC	13.5 s	12 s	11.2 s	9.9 s	10.5 s	9.3 s	6.12 s	5.76 s
FPPT	UIC	3.3 s	1.8 s	3 s	1.7 s	2.1 s	1.65 s	0.9 s	1 s
	PSC	2.1 s	9 s	1.6 s	8 s	1.5 s	7 s	1.36 s	4.6 s

* **T-1** is for start-up transition, **T-2** is for run-time transition .

performance of the linear STM is quite affected by the PSC. As can be observed in Table III, the MPPT takes 4.38 s and 3.54 s less time to converge during the start-up and run-time transitions, respectively, if the linear STM is replaced with D-MARS. The particular improvement is around 2.4 s in the case of the FPPT during the run-time transition. The amount of improvement with respect to the previous best time is also highest for the D-MARS controller in most of the cases. The performance of the D-MARS controller might have, yet, been somewhat deteriorated because of the hardware and measurement noises, as the physical MPPT under the PSC takes 1.6 s more time than the simulation during the start-up transition. This, in turn, indicates the possibility of further improving the performance of the D-MARS controller by using high precision sensors and properly designed printed circuit boards.

V. Conclusion

A novel D-MARS scheme has been proposed for the STM of the power tracking control so as to improve the overall speed of power tracking. The PTC sampling interval has been varied in accordance with the time that the converter needs to reach the steady-state after a duty ratio perturbation. However, unlike the existing approaches of studying the converter transient offline, the proposed STM has been performed by observing the actual converter transient during real-time power tracking. The steady state of the converter dynamics, following a duty-ratio perturbation, has been recognized by computing the moving variance of the PV array voltage samples collected through a high frequency sampler. A separate treatment has been made for the prolonged converter transient in the positive-slope region of the $P-V$ curve. Simple mathematical procedures have been established to tune the D-MARS controller parameters irrespective of the operating condition or the PV module product used to make the PV array. The proposed D-MARS scheme has been implemented in hardware and used with different sweeping and metaheuristic optimization-based MPPT and FPPT control techniques available in the literature. Results have proven the usefulness of the D-MARS controller to make the power tracking faster in comparison to other STM schemes. A prominent improvement in the power tracking speed has been observed in every case. The improvement was, in fact, very significant during the power tracking under partial shading.

References

[1] O. Khan and W. Xiao, "Integration of start–stop mechanism to improve maximum power point tracking performance in steady state," *IEEE Trans. Ind. Electron.*, vol. 63, no. 10, pp. 6126–6135, Oct. 2016.

[2] N. Kumar, I. Hussain, B. Singh, and B. K. Panigrahi, "Framework of maximum power extraction from solar PV panel using self predictive perturb and observe algorithm," *IEEE Trans. Sustain. Energy*, vol. 9, no. 2, pp. 895–903, Apr. 2018.

[3] P. Manoharan et al., "Improved perturb and observation maximum power point tracking technique for solar photovoltaic power generation systems," *IEEE Syst. J.*, vol. 15, no. 2, pp. 3024–3035, Jun. 2021.

[4] N. Swaminathan, N. Lakshminarasamma, and Y. Cao, "A fixed zone perturb and observe MPPT technique for a standalone distributed PV system," *IEEE J. Emerg. Sel. Topics Power Electron.*, vol. 10, no. 1, pp. 361–374, Feb. 2022.

[5] N. Kumar, I. Hussain, B. Singh, and B. K. Panigrahi, "Self-adaptive incremental conductance algorithm for swift and ripple-free maximum power harvesting from PV array," *IEEE Trans. Ind. Inform.*, vol. 14, no. 5, pp. 2031–2041, May 2018.

[6] A. Khazaee, A. Yazdani, H. M. Hesar, and B. Wu, "Efficient MPPT for BLDCM-driven PV pumping system based on ripple correlation control," *IEEE Trans. Ind. Inform.*, vol. 38, no. 7, pp. 8022–8026, Jul. 2023.

[7] H. D. Tafti et al., "Extended functionalities of photovoltaic systems with flexible power point tracking: Recent advances," *IEEE Trans. Power Electron.*, vol. 35, no. 9, pp. 9342–9356, Sep. 2020.

[8] A. Narang et al., "Dynamic reserve power point tracking in grid-connected photovoltaic power plants," *IEEE Trans. Power Electron.*, vol. 38, no. 5, pp. 5939–5951, May 2023.

[9] Q. Bi, G. Zhou, and Q. Tian, "Improved flexible power point tracking algorithm for PV system under fast-changing irradiance conditions," *IEEE Trans. Power Electron.*, vol. 38, no. 3, pp. 4061–4071, Mar. 2023.

[10] H. D. Tafti, G. Konstantinou, J. E. Fletcher, L. Callegaro, G. G. Farivar, and J. Pou, "Control of distributed photovoltaic inverters for frequency support and system recovery," *IEEE Trans. Power Electron.*, vol. 37, no. 4, pp. 4742–4750, Apr. 2022.

[11] M. K. K. Reddy and V. Sarkar, "The quantum-mode regulated power point tracking in a photovoltaic array for application under the quantised converter duty-ratio," *IET Renew. Power Gener.*, vol. 15, no. 5, pp. 1748–1764, Mar. 2021.

[12] A. Kumaresan, H. D. Tafti, N. K. Kandasamy, G. G. Farivar, J. Pou, and T. Subbaiyan, "Flexible power point tracking for solar photovoltaic systems using secant method," *IEEE Trans. Power Electron.*, vol. 36, no. 8, pp. 9419–9429, Aug. 2021.

[13] R. G. Merchan et al., "Binary search based flexible power point tracking algorithm for photovoltaic systems," *IEEE Trans. Ind. Electron.*, vol. 68, no. 7, pp. 5909–5920, Jul. 2021.

[14] J. Zhang et al., "Fast frequency regulation method for power system with two-stage photovoltaic plants," *IEEE Trans. Sustain. Energy*, vol. 13, no. 3, pp. 1779–1789, Jul. 2022.

[15] M. Ahmed et al., "Model-based maximum power point tracking algorithm with constant power generation capability and fast DC-link dynamics for two-stage PV systems," *IEEE Access*, vol. 10, pp. 48551–48568, 2022.

[16] S. Vanti, P. R. Bana, S. D. Arco, and M. Amin, "Single-stage grid-connected PV system with finite control set model predictive control and an improved maximum power point tracking," *IEEE Trans. Sustain. Energy*, vol. 13, no. 2, pp. 791–802, Apr. 2022.

[17] M. A. K. Magableh, A. Radwan, and Y. A. R. I. Mohamed, "Assessment and mitigation of dynamic instabilities in single-stage grid-connected photovoltaic systems with reduced DC-link capacitance," *IEEE Access*, vol. 9, pp. 55522–55536, 2021.

[18] M. Aquib, S. Jain, and V. Agarwal, "A time-based global maximum power point tracking technique for PV system," *IEEE Trans. Power Electron.*, vol. 35, no. 1, pp. 393–402, Jan. 2020.

[19] S. Ahmed et al., "An adaptive perturb and observe algorithm with enhanced skipping feature for fast global maximum power point tracking under partial shading conditions," *IEEE Trans. Power Electron.*, vol. 38, no. 9, pp. 11601–11613, Sep. 2023.

[20] H. Deboucha, M. Kermadi, S. Mekhilef, and S. L. Belaid, "Voltage track optimizer based maximum power point tracker under challenging partially shaded photovoltaic systems," *IEEE Trans. Power Electron.*, vol. 36, no. 12, pp. 13817–13825, Dec. 2021.

[21] H. D. Tafti, Q. Wang, C. D. Townsend, J. Pou, and G. Konstantinou, "Global flexible power point tracking in photovoltaic systems under partial shading conditions," *IEEE Trans. Power Electron.*, vol. 37, no. 9, pp. 11332–11341, Sep. 2022.

[22] A. Kumaresan et al., "Improved secant-based global flexible power point tracking in photovoltaic systems under partial shading conditions," *IEEE Trans. Power Electron.*, vol. 38, no. 8, pp. 10383–10395, Aug. 2023.

[23] M. K. K. Reddy and V. Sarkar, "Designing a generic multi-modality processing adapter for the practical implementation of the photovoltaic regulated power point tracking under the partial shading," *Electric Power Syst. Res.*, vol. 208, Apr. 2022, Art. no. 107806.

[24] Z. Bi, J. Ma, K. L. Man, J. S. Smith, Y. Yue, and H. Wen, "An enhanced 0.8 V_{OC}-model-based global maximum power point tracking method for photovoltaic systems," *IEEE Trans. Ind. Appl.*, vol. 56, no. 6, pp. 6825–6834, Nov./Dec. 2020.

[25] M. A. Ghasemi, H. M. Foroushani, and F. Blaabjerg, "Marginal power-based maximum power point tracking control of photovoltaic system under partially shaded condition," *IEEE Trans. Power Electron.*, vol. 35, no. 6, pp. 5860–5872, Jun. 2020.

[26] V. K. Kolakaluri, M. N. Aalam, and V. Sarkar, "Metaheuristics assisted efficiency maximizing flexible power point tracking of a photovoltaic array under the partial shading," *IEEE Trans. Energy Convers.*, vol. 38, no. 3, pp. 1576–1588, Sep. 2023.
[27] N. Pragallapati, T. Sen, and V. Agarwal, "Adaptive velocity PSO for global maximum power control of a PV array under nonuniform irradiation conditions," *IEEE J. Photovolt.*, vol. 7, no. 2, pp. 624–639, Mar. 2017.
[28] I. Shams, S. Mekhilef, and K. S. Tey, "Maximum power point tracking using modified butterfly optimization algorithm for partial shading, uniform shading, and fast varying load conditions," *IEEE Trans. Power Electron.*, vol. 36, no. 5, pp. 5569–5581, May 2021.
[29] D. S. Pillai, J. P. Ram, A. M. Y. M. Ghias, M. A. Mahmud, and N. Rajasekar, "An accurate, shade detection-based hybrid maximum power point tracking approach for PV systems," *IEEE Trans. Power Electron.*, vol. 35, no. 6, pp. 6594–6608, Jun. 2020.
[30] I. Pervez, I. Shams, S. Mekhilef, A. Sarwar, M. Tariq, and B. Alamri, "Most valuable player algorithm based maximum power point tracking for a partially shaded PV generation system," *IEEE Trans. Sustain. Energy*, vol. 12, no. 4, pp. 1876–1890, Oct. 2021.
[31] J. P. Ram, D. S. Pillai, N. Rajasekar, and S. M. Strachan, "Detection and identification of global maximum power point operation in solar PV applications using a hybrid ELPSO-P&O tracking technique," *IEEE J. Emerg. Sel. Topics Power Electron.*, vol. 8, no. 2, pp. 1361–1374, Jun. 2020.
[32] R. Motamarri and N. Bhookya, "JAYA algorithm based on Lévy flight for global MPPT under partial shading in photovoltaic system," *IEEE J. Emerg. Sel. Topics Power Electron.*, vol. 9, no. 4, pp. 4979–4991, Aug. 2021.
[33] M. A. Elgendy, B. Zahawi, and D. J. Atkinson, "Operating characteristics of the P&O algorithm at high perturbation frequencies for standalone PV systems," *IEEE Trans. Energy Convers.*, vol. 30, no. 1, pp. 189–198, Mar. 2015.
[34] J. Dadkhah and M. Niroomand, "Optimization methods of MPPT parameters for PV systems: Review, classification, and comparison," *J. Modern Power Syst. Clean Energy*, vol. 9, no. 2, pp. 225–236, Mar. 2021.
[35] K. V. Kumar and V. Sarkar, "A comparative study of different operating regions for performing the regulated power point tracking in photovoltaic systems," in *Proc. 10th Nat. Power Electron. Conf.*, 2021, pp. 1–6.
[36] S. B. Santra, D. Chatterjee, K. Kumar, M. Bertoluzzo, A. Sangwongwanich, and F. Blaabjerg, "Capacitor selection method in PV interfaced converter suitable for maximum power point tracking," *IEEE J. Emerg. Sel. Topics Power Electron.*, vol. 9, no. 2, pp. 2136–2146, Apr. 2021.
[37] X. Li, Y. Zhu, H. Wen, Y. Du, and W. Xiao, "Reference-voltage-line-aided power incremental algorithm for photovoltaic GMPPT and partial shading detection," *IEEE Trans. Sustain. Energy*, vol. 13, no. 3, pp. 1756–1770, Jul. 2022.
[38] J. Kivimäki, S. Kolesnik, M. Sitbon, T. Suntio, and A. Kuperman, "Revisited perturbation frequency design guideline for direct fixed-step maximum power point tracking algorithms," *IEEE Trans. Ind. Electron.*, vol. 64, no. 6, pp. 4601–4609, Jun. 2017.
[39] S. M. Mirhassani, S. Z. M. Golroodbari, S. M. M. Golroodbari, and S. Mekhilef, "An improved particle swarm optimization based maximum power point tracking strategy with variable sampling time," *Int. J. Elect. Power Energy Syst.*, vol. 64, pp. 761–770, Jan. 2015.
[40] Y. Jiang, J. A. A. Qahouq, and T. A. Haskew, "Adaptive step-size with adaptive-perturbation-frequency digital MPPT controller for a single sensor photovoltaic solar system," *IEEE Trans. Power Electron.*, vol. 28, no. 7, pp. 3195–3205, Jul. 2013.
[41] S. M. R. Tousi, M. H. Moradi, N. S. Basir, and M. Nemati, "A function-based maximum power point tracking method for photovoltaic systems," *IEEE Trans. Power Electron.*, vol. 31, no. 3, pp. 2120–2128, Mar. 2016.
[42] J. Mishra, S. Das, D. Kumar, and M. Pattnaik, "A novel auto-tuned adaptive frequency and adaptive step-size incremental conductance MPPT algorithm for photovoltaic system," *Int. Trans. Elect. Energy Syst*, vol. 31, no. 10, pp. 1–14, Feb. 2021.
[43] R. Kumar, S. Khandelwal, P. Upadhyay, and S. Pulipaka, "Global maximum power point tracking using variable sampling time and $p - v$ curve region shifting technique along with incremental conductance for partially shaded photovoltaic systems," *Sol. Energy*, vol. 189, pp. 151–178, Sep. 2019.
[44] M. Krell, M. Tabie, H. Wöhrle, and E. Kirchner, "Memory and processing efficient formula for moving variance calculation in EEG and EMG signal processing," in *Proc. Int. Congr. Neurotechnology Electron. Inform.*, Vilamoura, Algarve, Portugal, 2015, pp. 41–45.
[45] H. K. Mehta, H. Warke, K. Kukadiya, and A. K. Panchal, "Accurate expressions for single-diode-model solar cell parameterization," *IEEE J. Photovolt.*, vol. 9, no. 3, pp. 803–810, May 2019.

Vinay Kumar Kolakaluri joined Indian Institute of Technology Hyderabad, Telangana, India, in 2019. He is currently working toward the Ph.D. degree in electrical engineering, Indian Institute of Technology Hyderabad, Telangana, India.

His research interests are in the areas of grid-connected photovoltaic systems, digital control of power electronic systems, and renewable power control.

Mohammad Nair Aalam is currently working toward the Ph.D. degree in electrical engineering with the Center for Power Electronics Systems at Virginia Tech, Blacksburg, VA, USA.

Between 2022 and 2023, he was working as a Junior Research Fellow with the Department of Electrical Engineering, Indian Institute of Technology Hyderabad, Telangana, India. He is interested to work in the areas of high-density power converters, digital control of power electronic systems, and modeling and control of three-phase PWM converters.

Vaskar Sarkar (Member, IEEE) received the Ph.D. degree in electrical engineering from the Indian Institute of Technology Bombay, Mumbai, India, in 2009.

He is currently a Professor with the Department of Electrical Engineering, Indian Institute of Technology Hyderabad, Telangana, India. He works in the areas of flexible power point tracking of photovoltaic systems, grid integration of renewables, microgrid, and power system stability.